Structure, magnetism, and conductivity in epitaxial Ti-doped α-Fe$_2$O$_3$ hematite: Experiment and density functional theory calculations

T. Droubay,[1,*] K. M. Rosso,[1] S. M. Heald,[3] D. E. McCready,[2] C. M. Wang,[2] and S. A. Chambers[1]

[1]*Fundamental Science Directorate, Pacific Northwest National Laboratory, Richland, Washington 99352, USA*
[2]*Environmental Molecular Sciences Laboratory, Pacific Northwest National Laboratory, Richland, Washington 99352, USA*
[3]*Advanced Photon Source, Argonne National Laboratory, Argonne, Illinois 60439, USA*

We explore the feasibility of growing epitaxial Ti-doped α-Fe$_2$O$_3$ hematite in which Ti(IV) substitutes for Fe(III) preferentially in one magnetic sublattice but not the other. Such a structure has been predicted by first-principles theory to be energetically favorable, and is expected to yield interesting and useful magnetic and electronic properties. However, we find experimentally that a majority of Ti dopants disperse and occupy random cation sites in both magnetic sublattices. Density functional theory predicts that the magnetically ordered and magnetically random structures are nearly isoenergetic.

I. INTRODUCTION

Hematite is a spin-canted antiferromagnet in the bulk with d^5 high-spin Fe(III) cations.[1] The spins in adjacent cation bilayers are oriented antiparallel in the *ab* plane. That is, along the *c* axis, the spin orientation and layer structure can be represented schematically as $(O_3$-M_α-M_α-O_3-M_β-M_β-O_3-M_α-M_α-O_3-M_β-M_β-O_3-$\ldots)$, where M-M represents a cation bilayer and α and β refer to the two spin orientations. Replacement of alternating Fe layers with Ti in either the α or β spin sublattice leads to ilmenite (FeTiO$_3$), which is a wide band gap semiconducting antiferromagnet with a Néel temperature of 59 K.[2] Below the Néel temperature, the Fe(II) atoms within each cation bilayer are ferromagnetically coupled and are oriented parallel to the *c* axis. The spins in alternating Fe bilayers are oriented opposite one another leading to the antiferromagnetic designation. However, doping α-Fe$_2$O$_3$ (hematite) with Ti(IV) (a d^0 cation) may allow modifications of the electronic, magnetic, and chemical properties of the host lattice that are unique because of ordered structures that may form. In the doped regime $[(Ti_xFe_{1-x})_2O_3]$, the properties depend critically on the sites occupied by Ti. If d^0 Ti(IV) substitutes preferentially in a cation bilayer of one particular spin orientation (either M_α-M_α or M_β-M_β), then its presence will reduce the spin of that layer. In this case, the *total* spin will be nonzero, and should increase with increasing dopant concentration. In contrast, if Ti(IV) is randomly distributed throughout cation bilayers of both spin orientations, a dilute system with essentially zero net spin is expected. Recently, Ti:α-Fe$_2$O$_3$ and α-Fe$_2$O$_3$-FeTiO$_3$ solid solutions have been posited to exhibit interesting and beneficial effects in the fields of paleomagnetism,[1] thermoelectrics,[3] catalysis,[4] and spin electronics.[5,6] However, the actual microstructures of these materials, which directly determine the resulting properties, are not known.

Butler *et al.*[6] have used density functional theory (DFT) to predict the structural and electronic properties of Ti:α-Fe$_2$O$_3$. Their calculations suggest that Ti substitutes preferentially for Fe(III) cations in alternating cation bilayers, resulting in a ferrimagnetic semiconductor with an effective net magnetic moment of $4\mu_B$/Ti atom. Adding Coulomb repulsion to the local spin-density approximation (LSDA $+U$) predicted insulating behavior with Ti donor electrons being localized on a neighboring Fe site, effectively reducing these irons from +3 to +2 formal charge states.[5] Experimentally, however, investigation of Ti:α-Fe$_2$O$_3$ prepared via hydrothermal techniques and studied using neutron diffraction and Mössbauer spectroscopy suggested that the main mechanism of charge compensation was Fe(III) cation vacancy creation in which three Ti(IV) ions replace four Fe(III) ions in a defect cluster.[7] In this model, two-thirds of the dopants are substitutional and one-third are interstitial. This result is somewhat unexpected in light of the stability of the hematite-ilmenite solid solution and pure ilmenite structures. However, variability in the structure as well as magnetic, chemical, and charge ordering may be highly dependent upon the synthesis route. Moreover, Wilson *et al.*[8] found in computational studies of ilmenite a strong interplay between structural relaxation and the relative stabilities of the Fe(III) and Fe(II) charge states.

What is needed on the experimental front is a synthesis technique allowing the highest degree of control, accompanied by the elucidation of structure-function relationships, illuminated by state-of-the-art theoretical calculations. This ensemble of probes will allow the structures that form under ideal conditions to be characterized and correlated with magnetic and electronic properties. To this end, we have prepared high-quality epitaxial hematite thin films where a fraction of the Fe atoms have been replaced by Ti atoms.

II. EXPERIMENTAL DETAILS

Thin films of Ti-doped hematite $(Ti_xFe_{1-x})_2O_3$ ($x \leq \sim 0.15$) were deposited by oxygen-plasma-assisted molecular beam epitaxy (OPAMBE) on α-Al$_2$O$_3$(0001). Deposition of pure α-Fe$_2$O$_3$ thin films on this system have been described previously.[9] Pure Fe and Ti metal were evaporated using an electron-beam evaporator and a high-temperature effusion cell, respectively. Atomic oxygen was supplied from an electron cyclotron resonance oxygen plasma source with an integrated ion trap.

The back and sides of $10 \times 10 \times 1$ mm α-Al$_2$O$_3$(0001) substrates were etched in concentrated nitric acid to eliminate magnetic contamination from dicing. Room-temperature vibrating sample magnetometry (VSM) was used to verify a magnetically clean substrate prior to growth. The substrates were then ultrasonically cleaned in acetone and isopropyl alcohol, placed within a UV-ozone cleaner for 3 min, and inserted into ultrahigh vacuum. After introduction into the deposition chamber, the substrates were cleaned with atomic oxygen from an oxygen plasma beam at a chamber pressure of 2×10^{-5} torr for 30 min to rid the substrates of any residual adventitious carbon. The substrates were then annealed at ~ 550 °C in the oxygen plasma for an additional 15–30 min to improve the surface crystallinity.

Buffer layers of ~ 120-Å-thick Cr$_2$O$_3$ were first grown to grade the strain caused by the lattice mismatch between α-Fe$_2$O$_3$ and α-Al$_2$O$_3$.[9] All epitaxial films were grown at a substrate temperature of ~ 550 °C in excess atomic oxygen using a Fe metal evaporation rate of ~ 0.1 Å/s and a variable Ti flux to achieve the desired range of doping levels. The structural quality and surface morphology were monitored in real time using reflection high-energy electron diffraction (RHEED). Layer-by-layer epitaxial growth of the Cr$_2$O$_3$ buffer layer was established by observing intensity oscillations of the (00) RHEED spot. During the initial stages of doped hematite growth, RHEED intensity oscillations were seen for a few samples. The majority of samples, however, did not exhibit intensity oscillations. Therefore, step-flow growth tended to dominate over nucleation and coalescence of islands in the layer-by-layer growth mode. Final RHEED patterns of (Ti$_x$Fe$_{1-x}$)$_2$O$_3$ films did not vary in quality substantially from those of pure α-Fe$_2$O$_3$. Immediately following growth, the oxygen flux was stopped and the sample cooled to prevent Ti diffusion to the surface. Extensive dopant diffusion in the oxygen plasma has been seen in a separate doped oxide system, Co-doped TiO$_2$ anatase.[10]

In situ x-ray photoelectron spectroscopy (XPS), located in an appended analysis chamber, was utilized to assist in the determination of formal valence states of the cations as well as approximate the Ti concentration. Dopant concentrations were determined by energy dispersive x-ray (EDX) analysis accompanying transmission electron microscopy (TEM) and proton-induced x-ray emission (PIXE). The crystalline structure of the film stack was analyzed by high-resolution x-ray diffraction (XRD) with a four-circle goniometer while film thickness and roughness was measured using x-ray reflectivity (XRR). *K*-edge x-ray absorption near-edge spectra (XANES) and extended x-ray absorption fine-structure (EXAFS) were measured on the PNC-CAT beamline at the Advanced Photon Source at Argonne National Laboratory and used to determine dopant charge state and local structure. Magnetic properties were measured at room temperature with a Lakeshore 7404 VSM. Magnetic measurements were made with the magnetic field parallel to the plane of the film.

III. COMPUTATIONAL DETAILS

The purpose of the calculations was to evaluate the lattice distortion, total energies, and densities of states accompany-

ing Ti(IV) substitution for Fe(III) in the hematite lattice. *Ab initio* energy minimizations of the bulk hematite structure with and without Ti dopants were performed using periodic boundary conditions and the program CRYSTAL03.[11] CRYSTAL is a linear combination of atomic orbitals program that builds crystalline orbitals from a linear combination of space-symmetry adapted Bloch functions that are defined in terms of local Gaussian functions. The self-consistent field calculation is performed in reciprocal space.

With CRYSTAL calculations, the basis set must be carefully chosen to avoid overly diffuse functions and quasilinear dependence of the Bloch functions. The proper approach is to first optimize the basis set exponents and coefficients given the experimentally known lattice parameters and atomic coordinates. Basis sets for Fe and O prepared in this way were taken from the literature.[12] These are based on the Durand[13] $21d41G$ electron core pseudopotential (ECP) CRYSTAL basis set of Catti and co-workers, and the Durand41G ECP CRYSTAL basis set of Apra.[14] Both use ECP's of Durand and Barthelat;[15] for iron it is a large core ECP (i.e., only $4s$, $4p$, and $3d$ orbitals are treated explicitly). We developed a similar basis set for Ti(IV) and optimized all exponents and coefficients using the experimental rutile structure.

We performed wave-function calculations and geometry optimizations using density functional theory in the Kohn-Sham strategy[16] with the hybrid functional B3LYP.[17] Spin-unrestricted solutions were obtained, using the known antiferromagnetic structure of hematite in the initial guess. A $2 \times 2 \times 1$ supercell of the conventional hematite lattice (containing 48 metal sites) was used to allow for lower Ti:Fe ratios and to increase the spacing between Ti dopants between image cells. To reduce the computational cost, we imposed the $P3$ space group, with the dopant site(s) chosen to lie on the threefold axis parallel to the [001] direction. All atomic coordinates and unit cell parameters were first optimized for the hematite lattice. Upon Ti(IV) substitution into the cell, only atomic coordinates were optimized. Net charge on the Ti-substituted unit cell was eliminated from the Ewald summation by subtracting a uniform background charge density.

IV. RESULTS AND DISCUSSION

The morphological and structural quality of the resulting films is apparent in the TEM cross-sectional lattice images seen in Fig. 1 for a film with $x=0.035$. The Cr$_2$O$_3$ buffer layer as well as the (Ti$_x$Fe$_{1-x}$)$_2$O$_3$ film are highly epitaxial with the orientation of HR-TEM micrographs and associated EDX spectra confirming that both (Ti$_x$Fe$_{1-x}$)$_2$O$_3$/Cr$_2$O$_3$ and Cr$_2$O$_3$/Al$_2$O$_3$ interfaces are abrupt. The amorphous surface layer seen in Fig. 1(b) is due to the ion-milling procedure used to thin the sample as RHEED patterns following growth show a purely crystalline surface region prior to TEM sample preparation. (Typical RHEED patterns are shown in Fig. 2.) The Ti and Fe cation concentrations determined by EDX ($x=0.035$) were confirmed by PIXE ($x=0.027$), with excellent agreement between the two methods.

High-resolution XRD and RHEED results are shown in Fig. 2. Two distinct x-ray Bragg peaks are visible at Ω
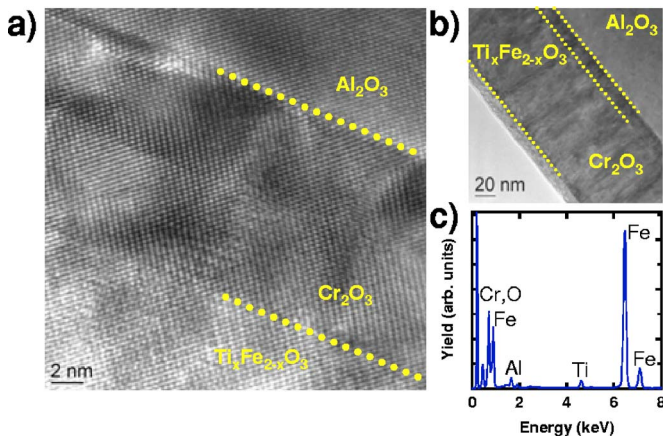
FIG. 1. (Color online) High- (a) and low- (b) resolution cross-sectional TEM micrographs for the epitaxial $(Ti_xFe_{1-x})_2O_3/Cr_2O_3/Al_2O_3(0001)$ interface for which $x=0.035$, along with the EDX spectrum measured with the beam centered in the $(Ti_xFe_{1-x})_2O_3$ layer (c).

$=\sim 19.5°$ and 20.8° [Fig. 2(a)], corresponding to Fe_2O_3 and Al_2O_3. The $\sim 0.1°$ discrepancy between the Bragg angle observed at 19.5° and that expected for pure Fe_2O_3 suggests that the observed peak is due to the presence of $(Ti_xFe_{1-x})_2O_3$. Weaker Bragg features appear to be present at $\Omega = \sim 19.8°$ and $\sim 19.2°$ but these are masked by finite-thickness interference fringes or Laue oscillations. The two weaker Bragg features are quite close to those associated with Cr_2O_3 and $TiFeO_3$, respectively, and the latter suggests the presence of a $TiFeO_3$-type ordered minority phase along with $(Ti_xFe_{1-x})_2O_3$. In ilmenite, the ordering of Fe(II) and Ti(IV) in alternate cation layers reduces the symmetry from $R\bar{3}c$ to $R\bar{3}$. This reduction of symmetry provides the basis for the designation of a $TiFeO_3$-type phase rather than the series
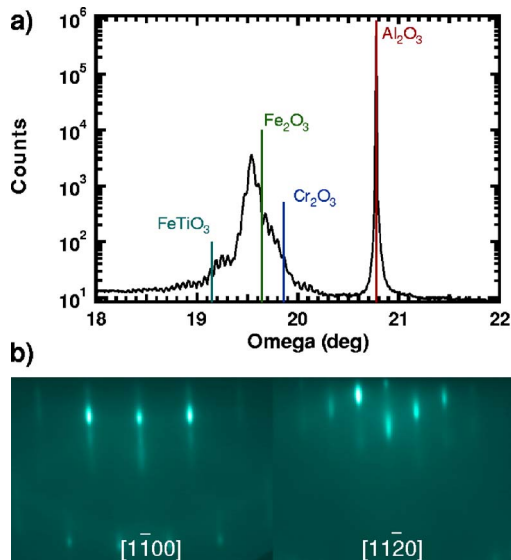

FIG. 2. (Color online) High-resolution XRD scan for $(Ti_{0.07}Fe_{0.93})_2O_3/Cr_2O_3/\alpha$-$Al_2O_3(0001)$ (a), and typical RHEED patterns after cooldown for $(Ti_{0.04}Fe_{0.96})_2O_3/Cr_2O_3/\alpha$-$Al_2O_3(0001)$ along the $[1\bar{1}00]$ and $[11\bar{2}0]$ azimuths (b).
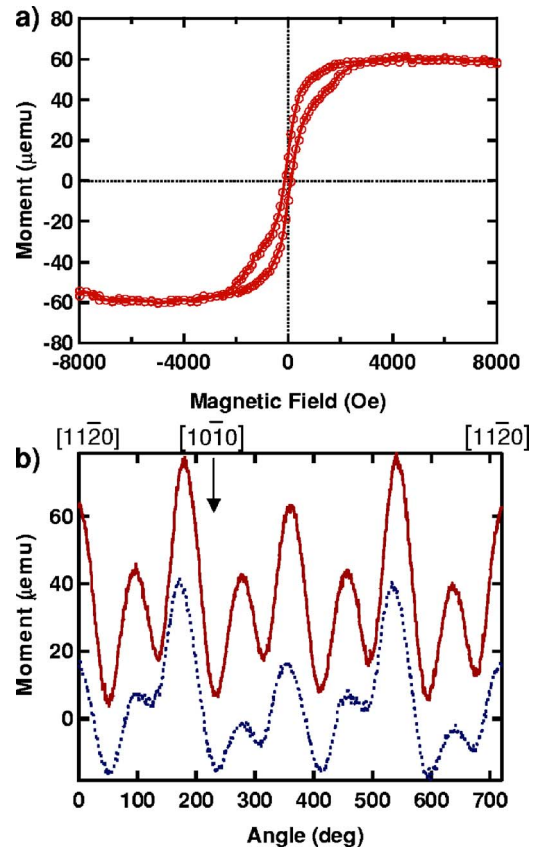

FIG. 3. (Color online) Typical VSM hysteresis loop measured at room temperature for $(Ti_{0.08}Fe_{0.92})_2O_3/Cr_2O_3/\alpha$-$Al_2O_3(0001)$ with the magnetic field in the plane of the film (a), and the angular dependence of the magnetic moment measured at magnetic fields of 1000 Oe (broken) and 4000 Oe (solid) (b).

endpoint $FeTiO_3$. The observed XRD spectrum lacks the (003) Bragg peak, which is allowed in ilmenite, but formally forbidden in hematite. Laue oscillations accompanying the film Bragg peaks reveal that the crystalline quality is excellent throughout the entire thickness, as corroborated by both HR-TEM and the low minimum yields in Rutherford backscattering spectrometry (RBS). There is no indication of either Ti or Fe interstitials throughout the bulk of the film from RBS. However, RBS in the channeling geometry reveals increased backscattering at the surface and interface of the film. This result is usually indicative of strain relief and the associated lateral lattice shifts resulting from misfit dislocation generation. The RHEED patterns seen in Fig. 2(b) are characterized by streaks with some intensity modulation, revealing some surface roughness, not unexpected considering the sizable lattice mismatches between the two film materials and the substrate.

We show in Fig. 3(a) an in-plane room-temperature VSM hysteresis curve for a $Ti_{0.04}Fe_{1.96}O_3$ film, which displays a saturation magnetization of $\sim 0.5\mu_B/Ti$. The hysteresis curve displays a dual-lobe structure typical of all films. The saturation magnetization was found to range from 0.37 to $0.72\mu_B/Ti$ over many films of different x, with an arithmetic mean and standard deviation of 0.5 and $0.15\mu_B/Ti$, respectively. This moment is a fraction of that expected if a ferro-

magnetically ordered layered phase had exclusively nucleated. At the same time, $0.5\mu_B$/Ti exceeds what is expected if the Ti distribution was perfectly random. This result suggests that a minority ($\sim 1/8$) of the Ti forms an ordered phase, the remainder being randomly distributed, consistent with the XRD. This conclusion is also supported by the fact that the hysteresis loops exhibit a dual-lobe structure that is best interpreted as two microstructurally distinct regions. This dual-lobed hysteretic behavior has been seen previously in hematite-ilmenite solid solutions.[18] Interestingly, these two phases have the same easy axis within the basal plane, but have different anisotropy constants. We show in Fig. 3(b) the in-plane rotational dependence of the magnetization. In these experiments, the longitudinal moment of the sample was measured while the sample was rotated in magnetic fields of ~ 4 kG and ~ 1 kG. The 4 kG field saturates the sample along the easy axis—[01$\bar{1}$0]. The ~ 1 kG field saturates the low coercivity phase only. The easy axes for the high coercivity phase lie along the same principal axes as those of the low coercivity phase, but the former has a stronger magnetocrystalline anisotropy constant. The low saturation moment in combination with the dual-lobed hysteresis loops and inequivalent in-plane anisotropies is consistent with a two magnetic phase system.

The electronic properties of the Ti-doped hematite films were examined *in situ* using XPS. As might be expected, the formal charge state of Ti for all x is Ti(IV) as determined both by Ti $2p$ core-level photoemission and Ti K-edge XANES. However, the formal valence state of Fe was dependent upon the concentration of the Ti dopant. Figure 4(a) shows Fe $2p$ core-level spectra as a function of x. The line shape is identical to that of pure hematite for $x < 0.15$, revealing exclusive Fe(III).[19] At $x=0.15$, a weak Fe(II) feature appears at ~ 708 eV and the intensity of the charge transfer satellite at ~ 719 eV decreases.[20] Interestingly, the appearance of a mid-gap state in the x-ray valence band photoemission spectra [Fig. 4(b)] also appears at $x=0.15$. The binding energy of this feature (~ 1.2 eV) agrees quite well that observed by Lad and Henrich[21] and assigned to Fe(II) for Fe$_x$O and Fe$_3$O$_4$. The absence of this feature for $x < 0.15$ may be due to three possible phenomena. First, the Ti(IV)-derived donor electrons may be itinerant for low x. However, while the resistivity drops somewhat with increasing x (ρ drops to ~ 25 Ω cm at $x=0.11$), it never reaches levels expected for an electronically doped semiconductor (fractions of an Ω cm). Second, each Ti(IV)-derived donor electron may be delocalized over many Fe cations at low x, such that the average extent of Fe reduction is very small and not detectable by XPS. In this scenario, more localization may occur with increasing x until each donor electron resides on a specific Fe cation, thereby reducing that cation to Fe(II). Third, one-to-one localization of donor electrons on Fe sites occur for all x, but XPS is not sufficiently sensitive to it for $x < 0.15$. We conjecture that the second explanation is most reasonable with the data at hand. In this case, the limited conductivity we observe, which increases with x, is due to electron hopping between Fe(II) and Fe(III) sites, similar to what occurs in magnetite (Fe$_3$O$_4$).

In order to confirm the cation charges and determine the local structure surrounding the Ti dopants we turn to K-shell
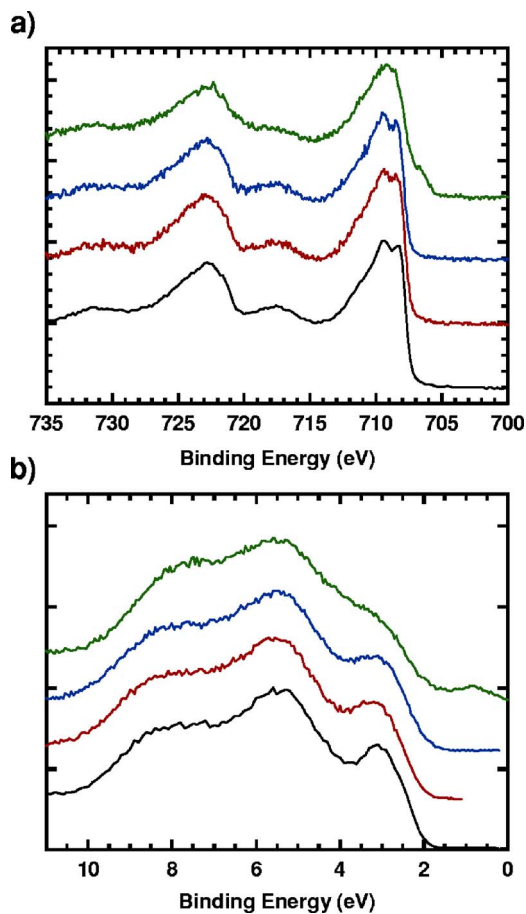

FIG. 4. (Color online) Fe $2p$ core-level (a) and valence band (b) XPS spectra as a function of x. From bottom to top in each panel, the spectra correspond to undoped Fe$_2$O$_3$, (Ti$_{0.04}$Fe$_{0.96}$)$_2$O$_3$, (Ti$_{0.08}$Fe$_{0.92}$)$_2$O$_3$, and (Ti$_{0.15}$Fe$_{0.85}$)$_2$O$_3$.

XANES and EXAFS, respectively. Figures 5(a) and 5(b) show the Fe and Ti K-edge XANES for two different (Ti$_x$Fe$_{1-x}$)$_2$O$_3$ films. By comparing the inflection points of these films with those of Fe, Fe$_3$O$_4$, and Fe$_2$O$_3$ standards [Fig. 5(a)], it is clear that Fe is in the $+3$ formal charge state in the films. This result confirms the designation of exclusively Fe(III) throughout the film. The Ti K-edge XANES line shape [Fig. 5(b)] very closely resembles that of the Fe K edge from the doped hematite films. Since the line shape depends primarily on the structure surrounding the absorbing atom, Ti(IV) appears to substitute for Fe(III). This result is supported by the Ti and Fe K-edge EXAFS, shown in Fig. 6, which confirms that the vast majority of Ti atoms occupy cation lattice sites. The raw EXAFS for the two K edges are essentially the same for $x=0.02$ and 0.04, as expected if Ti(IV) substitutes for Fe(III). Moreover, there is no evidence for interstitial Ti. Figure 6(b) shows a fit of the Fourier transform of the Ti K-shell EXAFS to a model FEFF calculation[22] for $x=0.04$. The best fit to the data is obtained assuming Ti substitution for Fe. The optimized Ti-O bond lengths are 1.91 ± 0.01 Å and 2.06 ± 0.02 Å for the short (R_1) and long (R_2) bonds, respectively. The analogous (Fe-O) bond lengths in pure hematite are 1.95 and 2.12 Å, while those for Ti-O bonds in ilmenite are 1.87 and 2.09 Å. The fact that R_1 for
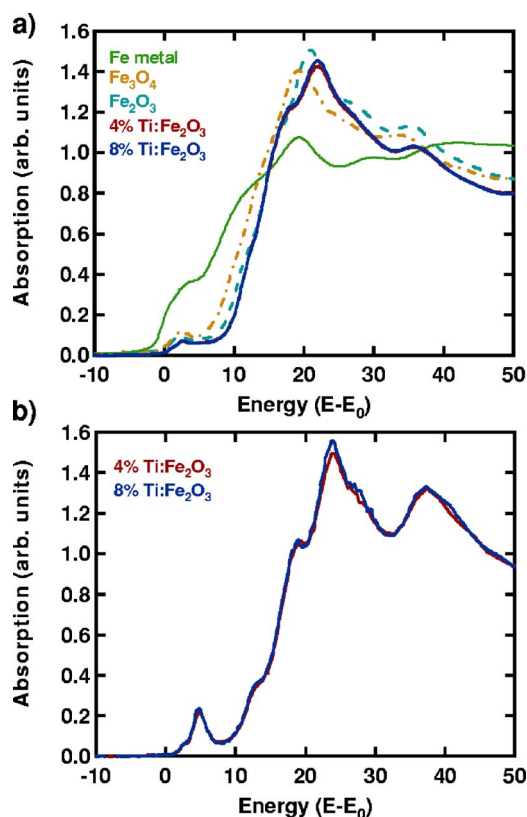
FIG. 5. (Color online) (a) Fe K-edge XANES spectra for 4% Ti:Fe_2O_3 and 8% Ti:Fe_2O_3, as well as standards of Fe metal (thin solid line), Fe_2O_3 (dashed line), and Fe_3O_4 (dashed-dotted line). The inflection-point energies of both Ti:Fe_2O_3 spectra match that for Fe_2O_3, indicating Fe is present as Fe(III) in Ti:Fe_2O_3. (b) Ti K-edge XANES spectra for 4% Ti:Fe_2O_3 and 8% Ti:Fe_2O_3 indicating the exclusive Ti(IV) formal valence state as well as line-shape similarity with Fe_2O_3.

FIG. 6. (Color online) (a) Raw Ti and Fe K-shell EXAFS data for pure α-Fe_2O_3 (solid), $(Ti_{0.02}Fe_{0.98})_2O_3$ (circles), and $(Ti_{0.04}Fe_{0.96})_2O_3$ (squares); (b) k^2-weighted Ti K-edge EXAFS data for the 4% sample (circles) and fit to the data by FEFF calculations assuming Ti is substitutional in hematite (solid line).

the films is bracketed by R_1 for pure hematite and ilmenite is suggestive of most of the Ti being randomly distributed at cation sites in Ti:α-Fe_2O_3. Moreover, better fits to the higher shells were obtained with hematite than ilmenite structures, consistent with randomly distributed Ti:α-Fe_2O_3 being the majority phase.

To gain theoretical insight, DFT calculations using the hybrid B3LYP functional were performed to ascertain lattice distortions, total energies, and densities of states for Ti-doped hematite. Computational details are given in Sec. III. Using a $2\times2\times1$ supercell of the hematite lattice, four structures were optimized: (1) pure hematite; (2) hematite +1 substitutional Ti; (3) hematite +2 substitutional Ti atoms across a shared octahedral face; (4) hematite +2 substitutional Ti that straddle a vacant octahedral cavity. These configurations are shown in Fig. 7. The cell in Fig. 7(c) simulates a random distribution of Ti whereas that in Fig. 7(d) simulates the ilmenite-like structure in which Ti dopants preferentially occupy one particular magnetic sublattice.

Our calculations correctly predict pure hematite to be a charge-transfer insulator having a mixed O $2p$-Fe $3d$ valence band dominated by O $2p$ states and a mixed O $2p$-Fe $3d$ conduction band minimum dominated by Fe $3d$ states. This is consistent with recent DFT calculations using the local
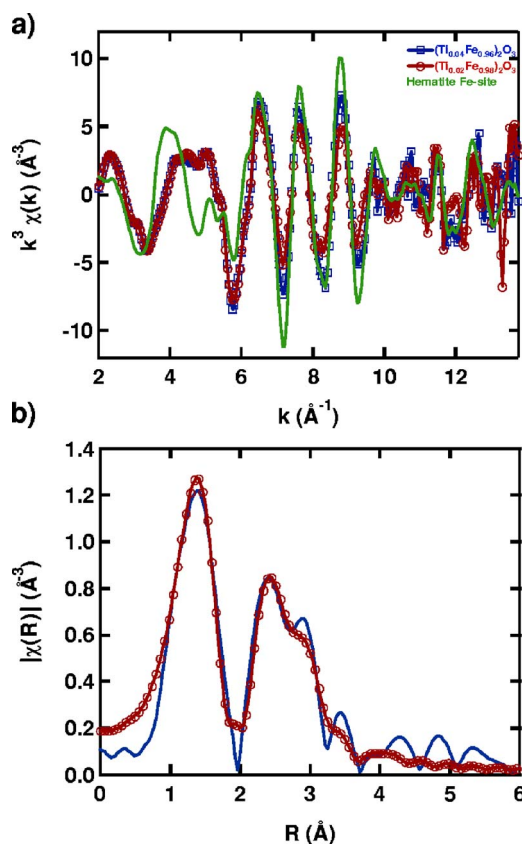
spin-density approximation, but only when the empirical Hubbard term U is included (LSDA+U).[5,6] In the LSDA $+U$ method, the U value dictates the magnitude of the energy penalty for double occupation of spin states, which tends to make the d states on Fe either pure spin up or spin down with increasing U. This both reduces the hybridization between occupied Fe d and O p states and corrects the strongly underestimated band gap typical of the LDA, yielding a charge-transfer insulator classification for hematite.[5] But this approach is only partially satisfying because the U value is arbitrary and typically adjusted *ad hoc* until the experimental band gap is reproduced by the calculation. In our calculations we rely on the hybrid functional B3LYP, which is an empirically derived correction to pure LDA exchange correlation, in part by incorporation of Hartree-Fock (exact) exchange. This approach yields a hematite band gap of 4.1 eV, substantially higher than the experimental value of $\sim$2.2 eV, but gives the correct description of the atomic orbital character of the valence band maximum and conduction band minimum and, as described below, very accurate predicted Ti-O bond lengths for substitution sites in structure.

A single Ti(IV) substitution for Fe(III) ($x=0.02$) leads to a computed band gap reduction of $\sim$0.2 eV relative to pure hematite due to the appearance of empty Ti $3d$ states just below but overlapping the conduction band minimum. The
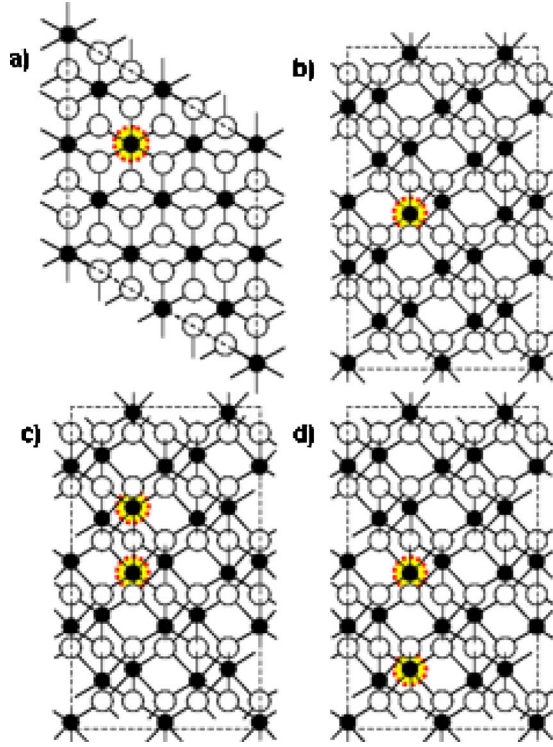
FIG. 7. (Color online) Depictions of the four scenarios and substitution sites considered in our calculations using the $2 \times 2 \times 1$ supercell: Pure hematite; [(a) and (b)] hematite +1Ti/Fe substitution; (c) hematite +2Ti/Fe substitutions with the two Ti atoms across a shared octahedral face; (d) hematite +2Hi/Fe substitutions with the two Ti atoms across a vacant octahedral cavity.

effect of two Ti substitutions ($x=0.04$) on the band gap depends on whether the two sites are across an octahedral face (i.e., they are located in adjacent metal bilayers) or whether they are across an octahedral cavity (i.e., are located in alternate metal bilayers). For two Ti substitutions across an octahedral face [Fig. 7(c)], the band gap is reduced by ~0.3 eV by the appearance of empty Ti 3d states just below the conduction band minimum. For two Ti substitutions across an octahedral cavity [Fig. 7(d)], the band gap reduction is ~0.2 eV. The computed total electronic energy difference between these two fully relaxed structures is 0.038 eV, with the Ti substitutions arranged across an octahedral face turning out to be more stable than for Ti substitutions across an octahedral cavity. This result is in contrast to that of Butler *et al.*,[6] which states that two Ti dopants would prefer not occupy adjacent Fe bilayer planes (i.e. the ilmenite-like phase is energetically more favorable). Because our calculated energy difference is only approximately half of kT at the film growth temperature, our DFT results do not predict strong preferential formation for ilmenite-like structures for values of $x \leq 0.04$. This is consistent with our experimental finding that a majority of Ti dopants disperse and occupy random cation sites in both magnetic sublattices for $x \leq 0.15$. The behavior must be different for very large values of x, such as for $x=0.5$, which yields ilmenite with its ordered alternating Fe and Ti metal bilayers.

The computed M-O bond lengths associated with Ti substitution were compared with experiment. We show in Table

TABLE I. Computed metal-oxygen interatomic bond distances associated with the Ti/Fe substitution for the various substitutional geometries along with the experimental parameters calculated by FEFF to best fit the experimental EXAFS data for several $(Ti_xFe_{1-x})_2O_3$ films deposited on Cr_2O_3/α-$Al_2O_3(0001)$. For reference, the values for pure hematite Fe_2O_3 are included.

	Short (R_1), Å	Long (R_2), Å
Pure hematite [Fig. 7(a)]		
Fe-O	1.994 (1.946[a])	2.103(2.116[a])
Hematite+1Ti [Fig. 7(b)]		
Ti-O	1.901	2.122
Hematite+2Ti [Fig. 7(c)]		
Ti-O	1.878	2.154
Ti-O	1.885	2.082
Hematite+2Ti [Fig. 7(d)]		
Ti-O	1.913	2.108
Ti-O	1.907	2.046
EXAFS		
Ti-O	1.91 +/−0.01	2.06+/−0.02

[a]Experimental values for pure hematite.

I the computed bond distances after total-energy minimization along with those obtained from the EXAFS. Comparing theory against experiment for pure hematite reveals differences of 0.048 and 0.013 Å for R_1 and R_2, respectively. The experimental values of R_1 and R_2 for Ti: α-Fe_2O_3 agree best with those of the ilmenite-like structure [Fig. 7(d)], for which the theory-experiment discrepancies (δ) are <0.02 Å. The levels of agreement for the isolated dopant [Figs. 7(a) and 7(b)] and random distribution [Fig. 7(c)] structures are the same for R_2 (δ=0.06 Å) and only slightly better for the isolated dopant on R_1 (δ=0.01 vs 0.03 Å). However, in light of the magnitudes of the theory/experiment discrepancies for pure hematite, we cannot say that theory favors one structure over the other.

V. CONCLUSIONS

In conclusion, MBE-grown $(Ti_xFe_{1-x})_2O_3(0001)$ consists of a majority phase in which Ti is randomly dispersed throughout the two magnetic sublattices. A minority of the Ti appears to form an ilmenite-like magnetically ordered phase, leading to a small but non-negligible in-plane saturation magnetization. Due to the small calculated energy difference (0.038 eV) between the random and magnetically ordered phases, no strong phase preference is expected during MBE growth. The donor electrons introduced when Ti(IV) substitutes for Fe(III) are localized on Fe sites, resulting in low conductivity. The nonzero saturation moment ascribed to the minority ilmenite-like phase together with the Ti-induced conductivity makes this material an attractive candidate for further studies of the effect of localized moments on carriers in oxide semiconductors. However, the room-temperature ferromagnetism in $(Ti_xFe_{1-x})_2O_3$ appears to be a natural consequence of d^0 Ti(IV) substituting for d^5 Fe(III) in a nonran-

dom fashion, and is not functionally dependent on carriers to mediate the exchange interaction between dopants. Therefore, $(Ti_xFe_{1-x})_2O_3$ might be best classified as a semiconductor that is ferromagnetic, but not a ferromagnetic semiconductor.

*Corresponding author; PNNL, P.O. Box 999, MSIN K8-93, Richland, WA 99352; FAX: (509)376-1044; Email address: tim.droubay@pnl.gov

[1] P. Robinson, R. J. Harrison, S. A. McEnroe, and R. B. Hargraves, Am. Mineral. **89**, 725 (2004).

[2] P. F. McDonald, A. Parasiris, R. K. Pandey, B. L. Gries, and W. P. Kirk, J. Appl. Phys. **69**, 1104 (1991).

[3] H. Muta, K. Kurosaki, M. Uno, and S. Yamanaka, J. Alloys Compd. **335**, 200 (2002).

[4] C. J. Sartoretti, B. D. Alexander, R. Solarska, W. A. Rutkowska, J. Augustynski, and R. Cerny, J. Phys. Chem. **109**, 13685 (2005).

[5] A. Bandyopadhyay, J. Velev, W. H. Butler, S. K. Sarker, and O Bengone, Phys. Rev. B **69**, 174429 (2004); J. Velev, A. Bandyopadhyay, W. H. Butler, and S. K. Sarker, *ibid.* **71**, 205208 (2005).

[6] W. H. Butler, A. Bandyopadhyay, and R. Srinivasan, J. Appl. Phys. **93**, 7882 (2003).

[7] F. J. Berry, C. Greaves, O. Helgason, J. McManus, H. M. Palmer, and R. T. Williams, J. Solid State Chem. **151**, 157 (2000).

[8] N. C. Wilson, J. Muscat, D. Mkhonto, P. E. Ngoepe, and N. M. Harrison, Phys. Rev. B **71**, 075202 (2005).

[9] S. A. Chambers, Y. Liang, and Y. Gao, Phys. Rev. B **61**, 13223 (2000).

[10] S. A. Chambers, S. Thevuthasan, R. F. C. Farrow, R. F. Marks, J. U. Thiele, L. Folks, M. G. Samant, A. J. Kellock, N. Ruzycki, D. L. Ederer, and U. Diebold, Appl. Phys. Lett. **79**, 3467 (2001).

[11] V. R. Saunders, R. Dovesi, C. Roetti, R. Orlando, C. M. Zicovich-Wilson, N. M. Harrison, K. Doll, B. Civalleri, I. J. Bush, P. D'Arco, and M. Llunell, *CRYSTAL03 User's Manual* (University of Torino, Torino, 2003).

[12] N. Iordanova, M. Dupuis, and K. M. Rosso, J. Chem. Phys. **122**, 144305 (2005).

[13] M. Catti, G. Valerio, and R. Dovesi, Phys. Rev. B **51**, 7441 (1995).

[14] E. Apra, Ph.D Thesis (University of Torino, 1992).

[15] P. Durand and J. C. Barthelat, Theor. Chim. Acta **38**, 283 (1975).

[16] W. Kohn and L. J. Sham, Phys. Rev. **140**, A1133 (1965).

[17] A. D. Becke, J. Chem. Phys. **98**, 5648 (1993).

[18] C. M. Carmichael, Proc. R. Soc. London, Ser. A **263**, 508 (1961).

[19] Y. Gao and S. A. Chambers, J. Cryst. Growth **174**, 446 (1997).

[20] T. Droubay and S. A. Chambers, Phys. Rev. B **64**, 205414(2001).

[21] R. J. Lad and V. E. Henrich, Phys. Rev. B **39**, 13478 (1989).

[22] J. J. Rehr, J. M. Deleon, S. I. Zabinsky, and R. C. Albers, J. Am. Chem. Soc. **113**, 5135 (1991).